Efficient Long-Range Attention Network for Image Super-resolution

Xindong Zhang[1,2,⋆], Hui Zeng[2,⋆], Shi Guo[1], and Lei Zhang[1,⋆⋆]

[1] Dept. of Computing, The Hong Kong Polytechnic University
[2] OPPO Research, China
{csxdzhang, csshiguo, cslzhang}@comp.polyu.edu.hk, cshzeng@gmail.com

Abstract. Recently, transformer-based methods have demonstrated impressive results in various vision tasks, including image super-resolution (SR), by exploiting the self-attention (SA) for feature extraction. However, the computation of SA in most existing transformer based models is very expensive, while some employed operations may be redundant for the SR task. This limits the range of SA computation and consequently the SR performance. In this work, we propose an efficient long-range attention network (ELAN) for image SR. Specifically, we first employ shift convolution (shift-conv) to effectively extract the image local structural information while maintaining the same level of complexity as 1x1 convolution, then propose a group-wise multi-scale self-attention (GMSA) module, which calculates SA on non-overlapped groups of features using different window sizes to exploit the long-range image dependency. A highly efficient long-range attention block (ELAB) is then built by simply cascading two shift-conv with a GMSA module, which is further accelerated by using a shared attention mechanism. Without bells and whistles, our ELAN follows a fairly simple design by sequentially cascading the ELABs. Extensive experiments demonstrate that ELAN obtains even better results against the transformer-based SR models but with significantly less complexity. The source code can be found at https://github.com/xindongzhang/ELAN.

Keywords: Super-Resolution, Long-Range Attention, Transformer

1 Introduction

Singe image super-resolution (SR) aims at reproducing a high-resolution (HR) output from its degraded low-resolution (LR) counterpart. In recent years, deep convolutional neural network (CNN) [23] based SR models [11, 12, 47, 29, 6, 50, 60, 46, 53] have become prevalent for their strong capability in recovering or generating [24, 54] image high-frequency details, showing high practical value in image and video restoration, transition and display. However, many CNN-based

---

⋆ Equal contribution
⋆⋆ Corresponding author

methods extract local features with spatially invariant kernels, which are inflexible to adaptively model the relations among pixels. In addition, to enlarge the receptive field, the CNN-based SR models tend to employ very deep and complicated network topology [60, 10, 64, 41, 40] to recover more details, resulting in much computational resource consumption.

Recently, the transformer based methods have shown impressive performance on natural language processing tasks [4, 14, 33, 43] for their strong ability on modeling the self-attention (SA) of input data. The great success of transformers on NLP has inspired researchers to explore their application to computer vision tasks, and interesting results have been shown on several high-level vision tasks [13, 26, 34, 35, 44, 52]. Generally speaking, the input image is first divided into non-overlapped patches with different scales as tokens, and then the local feature extraction and SA modules are applied to the collection of patches. Though SA has proven to be effective for high-level vision tasks, its complexity grows quadratically with the input feature size, limiting its utilization in low-level vision tasks such as SR, where the feature size is usually very large.

A few attempts have been made to reduce the computational cost of SA in the application of SR. Mei *et al.* [40] divided an image into non-overlapped patches for modeling local feature and SA independently, which however may introduce border effect and deteriorate the visual quality of restored images. SwinIR [28] follows the design of Swin Transformer [35], where the local feature is first extracted by two cascaded 1×1 convolutions and then SA is calculated within a small sized window (i.e., 8×8) with a shifting mechanism to build connections with other windows. However, local features extracted by 1×1 convolutions with small receptive field may produce weak feature representations to calculate the SA for long-range modeling. Furthermore, calculating SA with a small window size restricts the ability of modeling long-range dependency among image pixels. Restormer [58] calculates the SA with dependency on the channel space which remains applicable to large images. However, modeling dependency on channel space may sacrifice some useful spatial information of textures and structures which is important for reproducing high quality HR images.

In this paper, we aim to develop an effective and efficient way to exploit image long-range attention for image SR with a simple network architecture. The existing transformer-based models such as SwinIR [28] have many redundant and fragmented components which are not cost-effective for the SR task, such as relative position bias, masking mechanism, layer normalization, and several sub-branches created with residual shortcut. We therefore aim to build a highly neat and efficient SR model, where the LR to HR image mapping is simply built by stacking local feature extraction operations and SA sequentially. Two successive shift convolution (shift-conv) operations are used to efficiently extract local structural information, while a shift-conv has larger receptive field but shares the same arithmetic complexity as a 1×1 convolution. For SA calculation, we propose a group-wise multi-scale self-attention (GMSA) operator, which divides features into different groups of different window sizes and calculates SA separately. This strategy provides a larger receptive field than a small fixed-

size window for long-range attention modeling, while being more flexible than a large fixed-size window for reducing the computation resource cost. Furthermore, a shared attention mechanism is proposed to accelerate the calculation for successive GMSA modules. Arming with the shift-conv and GMSA with shared attention, an efficient long-range attention network, namely ELAN, is readily obtained for SR. Our contributions are summarized as follows:

1) We propose an efficient long-range attention block to model image long-range dependency, which is important for improving the SR performance.
2) We present a fairly simple yet powerful network, namely ELAN, which records new state-of-the arts for image SR with significantly less complexity than existing vision transformer based SR methods.

2   Related work

Numerous deep learning based image SR methods have been developed in the past decade. Here we briefly discuss the related work from the perspective of CNN-based methods and transformer-based methods.

2.1   CNN-based SR methods

CNN-based methods have demonstrated impressive performance in the SR task. SRCNN [11] makes the first attempt to employ CNN for image SR by learning a non-linear mapping from the bicubically upsampled LR image to the HR output with only three convolution layers. Kim *et al.* [20] deepened the network with VGG-19 and residual learning and achieved much better performance. Since the pre-upsampling strategy increases the amount of input data to CNN and causes large computational cost, FSRCNN [12] adopts a post-upsampling strategy to accelerate the CNN model. An enhanced residual block was proposed in [29] to train the deep model without batch normalization, and the developed EDSR network won the first prize of the NTIRE2017 challenge [1].

To build more effective models for SR, the recently developed methods tend to employ deeper and more complicated architectures as well as the attention techniques. Zhang *et al.* proposed a residual-in-residual structure coupled with channel attention to train a very deep network over 400 layers. Other works like MemNet [49] and RDN [62] are designed by employing the dense blocks [16] to utilize the intermediate features from all layers. In addition to increasing the depth of network, some other works, such as SAN [10], NLRN [30], HAN [41] and NLSA [40], excavate the feature correlations along the spatial or channel dimension to boost the SR performance. Our proposed ELAN takes the advantage of fast local feature extraction, while models the long-range dependency of features via efficient group-wise multi-scale self-attention.

2.2   Transformer-based SR methods

The breakthrough of transformer networks in natural language processing (NLP) inspired of use of self-attention (SA) in computer vision tasks. The SA mechanism in transformers can effectively model the dependency across data, and it has achieved impressive results on several high-level vision tasks, such as image classification [13, 26, 34, 35, 44, 52], image detection [8, 32, 35, 52], and segmentation [7, 35, 57, 63]. Very recently, transformer has also been applied to low-level vision tasks [28, 55, 58, 9]. IPT [9] is an extremely large pre-trained model for various low-level vision tasks based on the standard vision transformer. It computes both the local feature and SA on non-overlapped patches, which however may lose some useful information for reproducing image details. SwinIR [28] hence adapts the Swin Transformer [35] to image restoration, which combines the advantages of both CNNs and transformers. Though SwinIR has achieved impressive results for image SR, its network structure is mostly borrowed from the Swin Transformer, which is designed for high-level vision tasks. In particular, the network design of SwinIR is redundant for the SR problem, and it calculates SA on small fixed-size windows, preventing it from exploiting long-range feature dependency. Our proposed ELAN is not only much more efficient than SwinIR but also able to compute the SA in larger windows.

3   Methodology

In this section we first present the pipeline of our efficient long-range attention network (ELAN) for SR tasks, and then discuss in detail its key component, the efficient long-range attention block (ELAB).

3.1   Overall Pipeline of ELAN

The overall pipeline of ELAN is shown in Figure 1(a), which consists of three modules: shallow feature extraction, ELAB based deep feature extraction, and HR image reconstruction. The network follows a fairly simple topology with a global shortcut connection from the shallow feature extraction module to the output of deep feature extraction module before fed into the HR reconstruction module. In specific, given a degraded LR image $X_l \in \mathbb{R}^{3 \times H \times W}$, where H and W are the height and width of the LR image, respectively, we first apply the shallow feature extraction module, denoted by $H_{SF}(\cdot)$, which consists of only a single 3×3 convolution, to extract the local feature $X_s \in \mathbb{R}^{C \times H \times W}$:

$$X_s = H_{SF}(X_l) \tag{1}$$

where C is the channel number of the intermediate feature.

X_s then goes to the deep feature extraction module, denoted by $H_{DF}(\cdot)$, which is composed of M cascaded ELABs. That is:
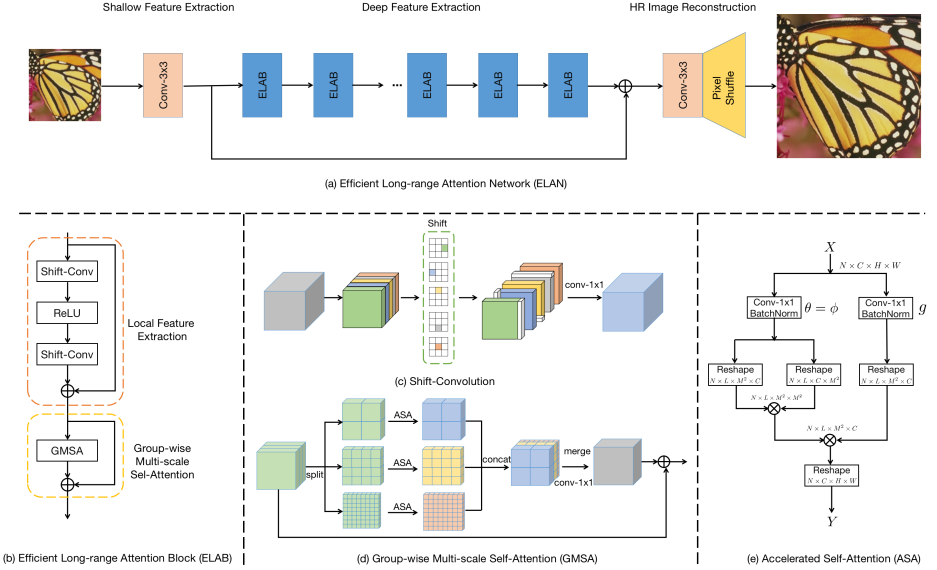
$$X_d = H_{DF}(X_s), \tag{2}$$

Fig. 1. Illustration of the proposed efficient long-range attention network (ELAN). (a) The overall pipeline of ELAN, which contains several ELABs, two 3×3 convolutions and one pixel shuffle operator. (b) The architecture of the efficient long-range attention block (ELAB). (c) Illustration of shift-conv, which is composed of a shift operation followed by one 1×1 convolution. (d) Illustration of the computation of group-wise multi-scale self-attention (GMSA). (e) Illustration of our accelerated self-attention (ASA) computation.

where $X_d \in \mathbb{R}^{C \times H \times W}$ denotes the output. By taking X_d and X_s as inputs, the HR image X_h is reconstructed as:

$$X_h = H_{RC}(X_s + X_d), \tag{3}$$

where H_{RC} is the reconstruction module. There are some choices for the design of the reconstruction module [11, 12, 47, 29]. To achieve high efficiency, we build it simply with a single 3×3 convolution and a pixel shuffle operation.

The ELAN can be optimized with the commonly used loss functions for SR, such as L_2 [11, 20, 48, 49], L_1 [22, 29, 62] and perceptual losses [16, 45]. For simplicity, given a number of N ground-truth HR images $\{X_{t,i}\}_{i=1}^{N}$, we optimize the parameters of ELAN by minimizing the pixel-wise L_1 loss:

$$\mathcal{L} = \frac{1}{N} \sum_{i=1}^{N} ||X_{h,i} - X_{t,i}||_1. \tag{4}$$

The Adam optimizer [21] is employed to optimize our ELAN for its good performance in low-level vision tasks.

3.2   Efficient Long-range Attention Block (ELAB)

As shown in Figure 1(b), our ELAB is composed of a local feature extraction module and a group-wise multi-scale attention (GMSA) module, both equipped with the residual learning strategy.

Local feature extraction. Given the intermediate features X, previous researches mostly extract the local features via multi-layer perception or two cascaded 1×1 convolutions, which however have only 1×1 receptive field. To enlarge the receptive field for more effective local feature extraction, we utilize two shift-conv [56] with a simple ReLU activation between them. As shown in Figure 1(c), the shift-conv is composed of a set of shift operations and one 1×1 convolution. Specifically, we split the input feature equally into five groups, and move the first four groups of feature along different spatial dimensions, including left, right, top, bottom, while the last group remains unchanged. Therefore, the followed 1×1 convolution can leverage information from neighboring pixels. Without introducing additional learnable parameters and much computation, shift-conv can provide larger receptive fields while maintaining almost the same arithmetic complexity as 1×1 convolution.

Group-wise multi-scale self-attention (GMSA). Given a feature map of $C \times H \times W$, the computational complexity of the window-based self-attention [35, 28] using $M \times M$ non-overlapped windows is $2M^2HWC$. The window size M determines the range of SA calculation, and a larger M contributes to exploit more self-similarity information. However, directly enlarging M will quadratically increase the computational cost and resources. To more efficiently calculate the long-range SA, we propose the GMSA module, which is illustrated in Figure 1(d). We first split the input feature X into K groups, denoted by $\{X_k\}_{k=1}^{K}$, then calculate SA on the k-th group of features using window size M_k. In this way, we can flexibly control the computational cost by setting the ratio of different window size. For example, supposing the K groups of features are equally split with $\frac{C}{K}$ channels, the computational cost of K groups of SA is $\frac{2}{K}(\sum_k M_k^2)HWC$. The SA calculated on different groups are then concatenated and merged via a 1×1 convolution.

Accelerated self-attention (ASA). The calculation of SA is computation and memory-intensive in existing transformer models [7, 35, 28, 55]. We make several modifications to accelerate the calculation of SA, especially in the inference stage. First, we discard the layer normalization (LN), which is widely employed in previous transformer models [7, 35, 28, 55], because the LN fragments the calculation of SA into many element-wise operations, which are not friendly for efficient inference. Instead, we utilize batch normalization (BN) [19] to stabilize the training process. It is worth mentioning that the BN can be merged into the convolution operation, which does not cause additional computation cost in the inference stage. Second, the SA in SwinIR [28] is calculated on the embedded Gaussian space, where three independent 1×1 convolutions, denoted by θ, ϕ and g, are employed to map the input feature X into three different feature maps. We set $\theta = \phi$ and calculate the SA in the symmetric embedded Gaussian space [30, 5], which can save one 1×1 convolution in each
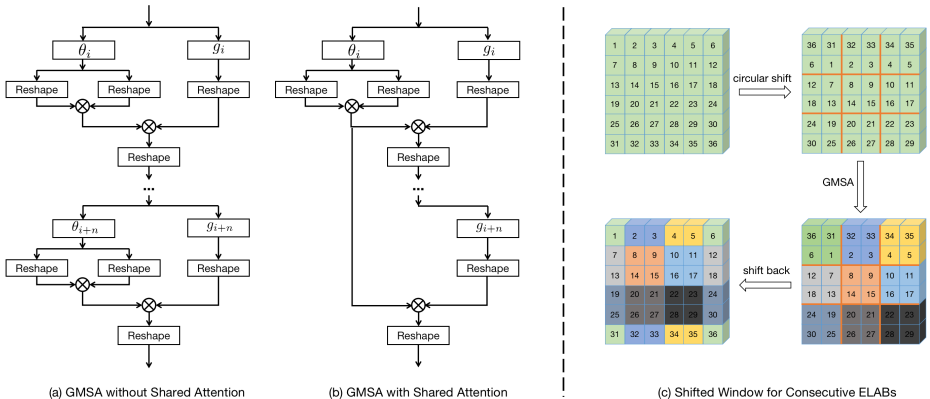
Fig. 2. (a) and (b) illustrate the calculation of GMSA without and with the shared attention mechanism, respectively. (c) Illustration of the shifted window mechanism used in consecutive ELABs.

SA. This modification further alleviates the computation and memory cost of SA without sacrificing the SR performance. Our ASA is shown in Figure 1(e).

Shared attention. Despite the above acceleration, one single forward pass of SA still consists of two 1×1 convolutions and four IO-intensive reshape operations. Although the reshape operation is FLOPs-free, it is time-consuming due to large feature size in the SR task. To further accelerate the SA computation of the entire network, we propose to share the attention scores among adjacent SA modules. As shown in Figure 2(b), the calculated attention scores in the i-th SA module is directly re-used by the following n SA modules on the same scale. In this way, we can avoid $2n$ reshape and n 1×1 convolution operations for the following n SAs. We found that the proposed shared attention mechanism only leads to slight drop in SR performance by using a a small number of n (e.g., 1 or 2), while it saves much computation resources during inference.

Shifted window. The calculated SA on the group-wise multi-scale windows still lacks connection across local windows within the same scale. We improve the shifted window mechanism of SwinIR [28] to reach a simple yet effective shifting scheme for the SR task. The whole process is visualized in Figure 2(c). We first employ circular shift to the feature along the diagonal direction and calculate GMSA on the shifted feature. Then we shift the result back via inverse circular shift. The circular shift with half window size leads to a new partition of feature map and introduces connections among neighboring non-overlapped windows in the previous GMSA module. Although some pixels on the border are shifted to distant areas via circular shift, we found it has negligible impact on the final SR performance since such pixels only occupy a small portion of the entire feature map in the SR task. Benefiting from the circular shift mechanism, we remove the masking strategy and relative positional encoding adopted in SwinIR [28], making our network neater and more efficient.

Table 1. Performance comparison of different light-weight SR models on five benchmarks. PSNR/SSIM on Y channel are reported on each dataset. #Params and #FLOPs are the total number of network parameters and floating-point operations, respectively. All the efficiency proxies (#Params, #FLOPs and Latency) are measured under the setting of upscaling SR images to 1280×720 resolution on all scales. Best and second best PSNR/SSIM indexes are marked in red and blue colors, respectively. The CNN-based methods and transformer-based methods are separated via a dash line for each scaling factor. '–' means that the result is not available.

Scale	Model	#Params (K)	#FLOPs (G)	Latency (ms)	Set5 [3] PSNR/SSIM	Set14 [59] PSNR/SSIM	B100[38] PSNR/SSIM	Urban100 [17] PSNR/SSIM	Manga109 [39] PSNR/SSIM
×2	CARN [2]	1,592	222.8	72	37.76/0.9590	33.52/0.9166	32.09/0.8978	31.92/0.9256	38.36/0.9765
	EDSR-baseline [29]	1370	316.3	71	37.99/0.9604	33.57/0.9175	32.16/0.8994	31.98/0.9272	38.54/0.9769
	IMDN [18]	694	158.8	54	38.00/0.9605	33.63/0.9177	32.19/0.8996	32.17/0.9283	38.88/0.9774
	LAPAR-A [25]	548	171.0	73	38.01/0.9605	33.62/0.9183	32.19/0.8999	32.10/0.9283	38.67/0.9772
	LatticeNet [37]	756	169.5	66	38.06/0.9607	33.70/0.9187	32.20/0.8999	32.25/0.9288	—/—
	ESRT [36]	677	—	—	38.03/0.9600	33.75/0.9184	32.25/0.9001	32.58/0.9318	39.12/0.9774
	SwinIR-light [28]	878	195.6	1007	38.14/0.9611	33.86/0.9206	32.31/0.9012	32.76/0.9340	39.12/0.9783
	ELAN-light (ours)	582	168.4	230	38.17/0.9611	33.94/0.9207	32.30/0.9012	32.76/0.9340	39.11/0.9782
×3	CARN [2]	1,592	118.8	39	34.29/0.9255	30.29/0.8407	29.06/0.8034	28.06/0.8493	33.50/0.9440
	EDSR-baseline [29]	1555	160.2	37	34.37/0.9270	30.28/0.8417	29.09/0.8052	28.15/0.8527	33.45/0.9439
	IMDN [18]	703	71.5	27	34.36/0.9270	30.32/0.8417	29.09/0.8046	28.17/0.8519	33.61/0.9445
	LAPAR-A [25]	544	114.0	55	34.36/0.9267	30.34/0.8421	29.11/0.8054	28.15/0.8523	33.51/0.9441
	LatticeNet [37]	765	76.3	33	34.40/0.9272	30.32/0.8416	29.10/0.8049	28.19/0.8513	—/—
	ESRT [36]	770	—	—	34.42/0.9268	30.43/0.8433	29.15/0.8063	28.46/0.8574	33.95/0.9455
	SwinIR-light [28]	886	87.2	445	34.62/0.9289	30.54/0.8463	29.20/0.8082	28.66/0.8624	33.98/0.9478
	ELAN-light (ours)	590	75.7	105	34.61/0.9288	30.55/0.8463	29.21/0.8081	28.69/0.8624	34.00/0.9478
×4	CARN [2]	1,592	90.9	30	32.13/0.8937	28.60/0.7806	27.58/0.7349	26.07/0.7837	30.47/0.9084
	EDSR-baseline [29]	1518	114.0	28	32.09/0.8938	28.58/0.7813	27.57/0.7357	26.04/0.7849	30.35/0.9067
	IMDN [18]	715	40.9	19	32.21/0.8948	28.58/0.7811	27.56/0.7353	26.04/0.7838	30.45/0.9075
	LAPAR-A [25]	659	94.0	47	32.15/0.8944	28.61/0.7818	27.61/0.7366	26.14/0.7871	30.42/0.9074
	LatticeNet [37]	777	43.6	23	32.18/0.8943	28.61/0.7812	27.57/0.7355	26.14/0.7844	—/—
	ESRT [36]	751	—	—	32.19/0.8947	28.69/0.7833	27.69/0.7379	26.39/0.7962	30.75/0.9100
	SwinIR-light [28]	897	49.6	271	32.44/0.8976	28.77/0.7858	27.69/0.7406	26.47/0.7980	30.92/0.9151
	ELAN-light (ours)	601	43.2	62	32.43/0.8975	28.78/0.7858	27.69/0.7406	26.54/0.7982	30.92/0.9150

4   Experiments

In this section, we conduct extensive experiments to quantitatively and qualitatively validate the superior performance of our ELAN for light-weight and classic SR tasks on five SR benchmark datasets. We also present comprehensive ablation studies to evaluate the design of our proposed ELAN.

4.1   Experimental setup

Dataset and evaluation metrics. We employ the DIV2K dataset [51] with 800 training images to train our ELAN model, and use the five benchmark datasets, including Set5[3], Set14[59], BSD100[38], Urban100[17] and Manga109[39], for performance comparison. PSNR and SSIM are used as the evaluation metrics, which are calculated on the Y channel after converting RGB to YCbCr format. For efficiency comparison, we report the latency evaluated on a single NVIDIA

2080Ti GPU in the inference stage. We also report the number of network parameters and FLOPs as reference, although they may not be able to faithfully reflect the network complexity and efficiency.

Note that since some competing methods do not release the source codes, we can only copy their PSNR/SSIM results from the original papers, but cannot report their results of latency and FLOPS.

Training details. Following SwinIR [28], we train two versions of ELAN with different complexity. The light-weight version, i.e., ELAN-light consists of 24 ELABs with 60 channels, while the normal version of ELAN has 36 ELABs with 180 channels. We calculate GMSA on three equally split scales with window size: 4×4, 8×8 and 16×16. By default, we set $n = 1$ for the shared attention mechanism. Bicubic downsampling is used to generate training image pairs. We randomly crop 64 patches of size 64×64, and 32 patches of size 48×48 from the LR images as training mini-batch for the light-weight and normal ELAN models, respectively. We employ randomly rotating $90°$, $180°$, $270°$ and horizontal flip for data augmentation. Both models are trained using the ADAM optimizer with $\beta_1 = 0.9$, $\beta_2 = 0.999$, and $\epsilon = 10^{-8}$ for 500 epochs. The learning rate is initialized as 2×10^{-4} and multiplied with 0.5 after $\{250, 400, 425, 450, 475\}$-th epoch. The model training is conducted by Pytorch [42] on NVIDIA 2080Ti GPUs.

4.2 Comparison with light-weight SR models

We first compare our ELAN-light with state-of-the-art light-weight SR models, including CNN-based models CARN[2], IMDN [18], LAPAR-A[25], LatticeNet[37], and transformer-based models ESRT [36] and SwinIR-light[28].

Quantitative comparison. The quantitative indexes of different methods are reported in Table 1. Several observations can be made from the table. First, with similar #Params and #FLOPs, the transformer-based methods especially SwinIR-light outperform much CNN-based methods on PSNR/SSIM indexes, by exploiting the self-similarity of images. However, the latency time of SwinIR-light is more than $\times 10$ slower than the CNN-based methods, because the calculation of self-attention in SwinIR is a heavy burden for inference. Benefiting from our efficient long-range attention design, our ELAN-light model not only obtains the best or second best PSNR/SSIM indexes on all the five datasets and on all the three zooming scales, but also is about $\times 4.5$ faster than SwinIR-light. Its #Params and #FLOPs are also smaller compared with SwinIR-light.

Qualitative comparison. We then qualitatively compare the SR quality of different light-weight models. The $\times 4$ SR results on six example images are shown in Figure 3 and Figure 4. One can see that all the CNN-based models result in blurry and distorted edges on most images. The transformer based SwinIR-light can recover the main structure in the 1st image and partial edges in the 2nd image of Figure 3, but cannot correctly restore the structures among the other four images (e.g., "Barbara", "img004", "img012" and "BokuHaSitatakaKun"). Our ELAN-light is the only method that can recover the main structures on most of the images with clear and sharp edges, demonstrating the effectiveness of our modeling of long-range self-attention for the SR task. It is worth mentioning
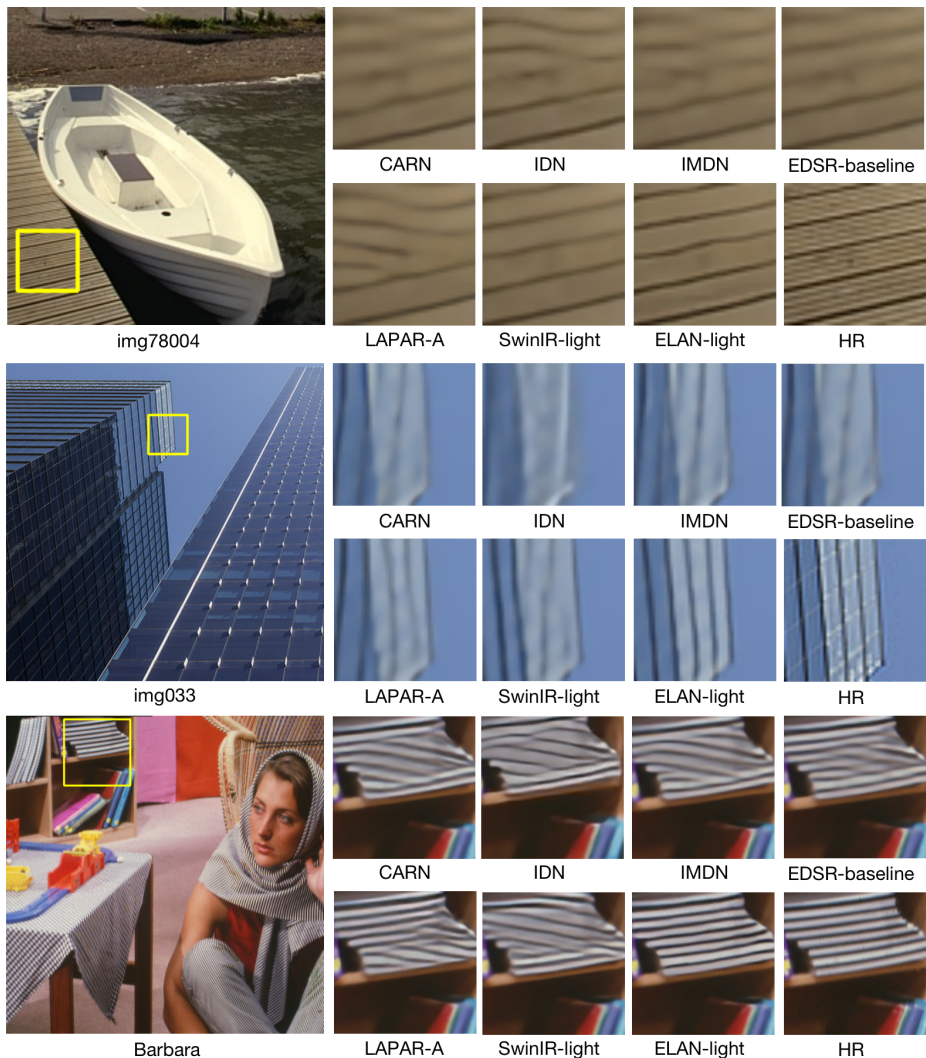
Fig. 3. Qualitative comparison of state-of-the-art light-weight SR models for ×4 up-scaling. ELAN-light can restore more accurate and clear structures than other models.

that the advantage of ELAN-light over SwinIR-light is achieved using much less computational cost, as we have validated in Table 1.

4.3   Comparison with classic SR models

To validate the scalability of ELAN, we further compare the normal version of ELAN with state-of-the-art classic performance-oriented SR models, including EDSR [29], SRFBN [27], RNAN [61], RDN [62], RCAN [31], SAN [10], IGNN
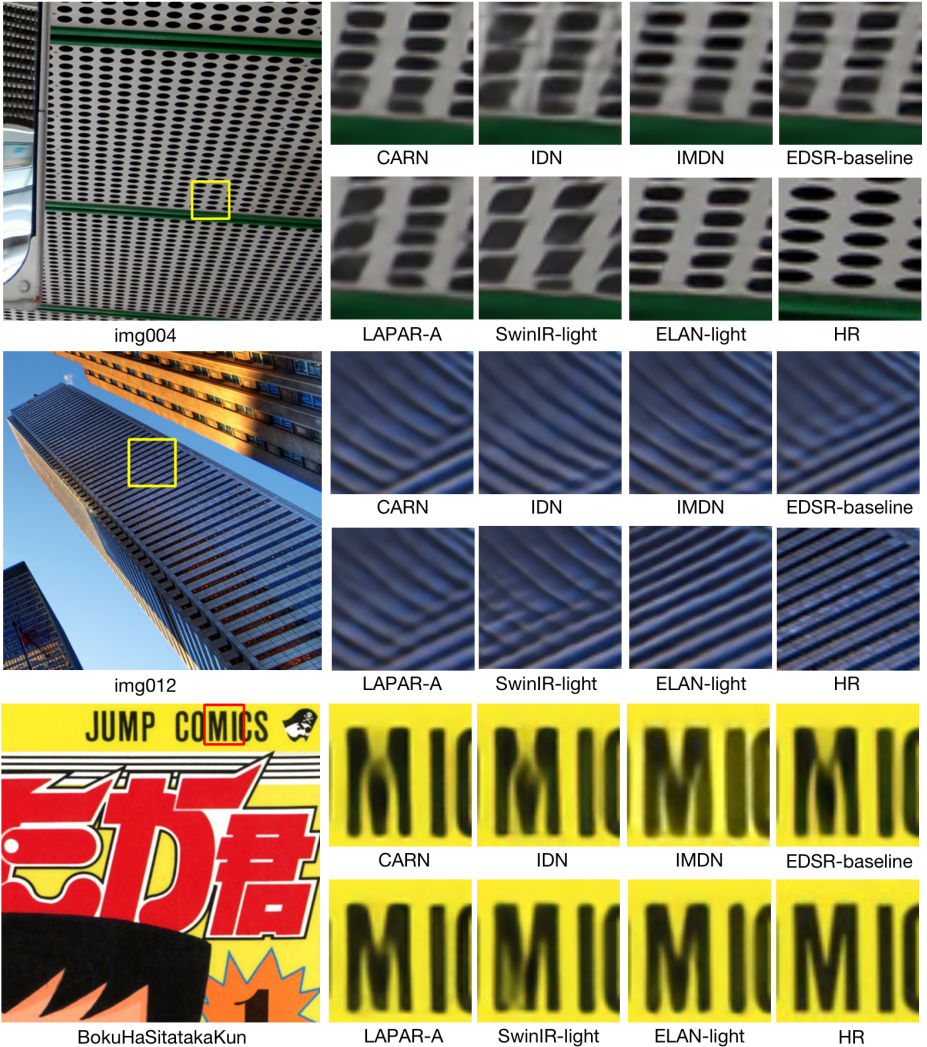
Fig. 4. Qualitative comparison of state-of-the-art light-weight SR models for ×4 upscaling. ELAN-light can restore more accurate and clear structures than other models.

[64], HAN [41], NLSA [40] and SwinIR [28]. Note that these models employ either very deep network topology with large channel number or complicated self-attention and non-local strategies.

Quantitative comparison. The quantitative results are shown in Table 2. As can be seen, our ELAN achieves the best results on almost all benchmarks and all upscaling factors. In particular, compared with SwinIR, our ELAN obtains better PSNR and SSIM indexes on almost all settings with less number of parameters and FLOPs, and more than ×2 faster inference speed. These performance

gains show that the proposed ELAB block succeeds in capturing useful information (such as long-range dependency) to conduct super-resolution in a more efficient and effective manner. Although the classical CNN-based SR models have huge amount of parameters and FLOPs, their performance is less competitive than the transformer-based models. Comparing with most CNN-based methods, our ELAN shows significant advantages in reconstruction performance metrics, benefiting from its larger receptive field and capability of modeling long-range spatial feature correlation. Some methods such as HAN and NLSA can also obtain competitive performance by exploiting dedicated attention mechanisms and very deep network, but their computation and memory cost are very expensive. For example, the NLSA model on ×2 upscaling task is too heavy to execute on a single NVIDIA 2080Ti GPU. Nevertheless, our ELAN obtains better performance than these complicated CNN-based models at much less cost.

Qualitative comparison. We compare the visual quality of SR results by our ELAN and six representative models, including EDSR [29], RDN [62], SAN [10], RCAN [62], IGNN [27] and SwinIR [28], on ×4 upscaling task. The results on six example images are shown in Figure 5 and Figure 6. One can first observe that most of the compared methods yield either blurry or inaccurate edges and textures (see the fur texture of the tiger body in Figure 5 and the edges on the skirt in Figure 6), while our ELAN can restore more accurate and sharper edges. The advantage of ELAN is more obvious on the images with repetitive patterns and edges (see the 2nd and 3rd images of of Figure 5 and 1st image of Figure 6). Most of the compared methods fail to reconstruct the correct structures, and even generate undesired artifacts. The transformer based methods such as SwinIR [28] can reproduce most of the patterns and edges in "img092" and "img003" but also suffer from artifacts and distortions in "img062" and "img092". In contrast, our ELAN can recover very clear patterns and edges in these examples. Referring to the last example in Figure 6 where the Chinese character consists of intensive strokes of many directions, our ELAN is the only model that can reproduce distinct edges among all strokes. These comparisons clearly demonstrate the advantage of ELAN in recovering image structures and details from low-resolution inputs.

4.4   Ablation studies

To better understand how ELAN works, we present comprehensive ablation studies to evaluate the roles of different components of ELAN, as well as the depth selection for the shared attention mechanism.

The components of ELAN. We first utilize the architecture and setting of ELAN-light to ablate the roles of different components of ELAB, and observe the change in performance and efficiency. The PSNR/SSIM indexes on five benchmarks and inference time of variant models are reported in Table 3. The indexes of SwinIR-light is also listed for reference. Specifically, we start with a naive baseline by removing the redundant sub-branches from SwinIR-light, where the deep feature extraction module is composed of 24 sequential swin transformer block. As expected, this simplification leads to slight performance

Table 2. Performance comparison of different classic performance-oriented SR models on five benchmarks. PSNR/SSIM on Y channel are reported on each dataset. #Params and #FLOPs are the total number of network parameters and floating-point operations, respectively. Noted that all the efficiency proxies (#Params, #FLOPs and Latency) are measured under the setting of upscaling SR images to 1280×720 resolution on all scales. Best and second best PSNR/SSIM indexes are marked in red and blue colors, respectively. The CNN-based methods and transformer-based methods are separated by a dash line. 'NaN' indicates that corresponding models are too heavy to run on a single NVIDIA 2080Ti GPU. '−' means that the result is not available.

Scale	Model	#Params (K)	#FLOPs (G)	Latency (ms)	Set5 [3] PSNR/SSIM	Set14 [59] PSNR/SSIM	B100[38] PSNR/SSIM	Urban100 [17] PSNR/SSIM	Manga109 [39] PSNR/SSIM
×2	EDSR [29]	40730	9387	1143	38.11/0.9602	33.92/0.9195	32.32/0.9013	32.93/0.9351	39.10/0.9773
	SRFBN [27]	2140	5044	920	38.11/0.9609	33.82/0.9196	32.29/0.9010	32.62/0.9328	39.08/0.9779
	RNAN [61]	9107	NaN	NaN	38.17/0.9611	33.87/0.9207	32.32/0.9014	32.73/0.9340	39.23/0.9785
	RDN [62]	22123	5098	846	38.24/0.9614	34.01/0.9212	32.34/0.9017	32.89/0.9353	39.18/0.9780
	OISR [15]	41910	9657	—	38.21/0.9612	33.94/0.9206	32.36/0.9019	33.03/0.9365	—
	RCAN [62]	15445	3530	743	38.27/0.9614	34.12/0.9216	32.41/0.9027	33.34 0.9384	39.44/0.9786
	SAN [10]	15861	3050	NaN	38.31/0.9620	34.07/0.9213	32.42/0.9028	33.10/0.9370	39.32/0.9792
	IGNN [64]	49513	—	—	38.24/0.9613	34.07/0.9217	32.41/0.9025	33.23/0.9383	39.35/0.9786
	HAN [41]	63608	14551	2278	38.27/0.9614	34.16/0.9217	32.41/0.9027	33.35/0.9385	39.46/0.9785
	NLSA [40]	41796	9632	NaN	38.34/0.9618	34.08/0.9231	32.43/0.9027	33.42/0.9394	39.59/0.9789
	SwinIR [28]	11752	2301	2913	38.35/0.9620	34.14/0.9227	32.44/0.9030	33.40/0.9393	39.60/0.9792
	ELAN (ours)	8254	1965	1244	38.36/0.9620	34.20/0.9228	32.45/0.9030	33.44/0.9391	39.62/0.9793
×3	EDSR [29]	43680	4470	573	34.65/0.9280	30.52/0.8462	29.25/0.8093	28.80/0.8653	34.17/0.9476
	SRFBN [27]	2833	6024	672	34.70/0.9292	30.51/0.8461	29.24/0.8084	28.73/0.8641	34.18/0.9481
	RNAN [61]	9292	809	NaN	34.66/0.9290	30.52/0.8462	29.26/0.8090	28.75/0.8646	34.25/0.9483
	RDN [62]	22308	2282	406	34.71/0.9296	30.57/0.8468	29.26/0.8093	28.80/0.8653	34.13/0.9484
	OISR [15]	44860	4590	—	34.72/0.9297	30.57/0.8470	29.29/0.8103	28.95/0.8680	—
	RCAN [62]	15629	1586	367	34.74/0.9299	30.65/0.8482	29.32/0.8111	29.09/0.8702	34.44/0.9499
	SAN [10]	15897	1620	NaN	34.75/0.9300	30.59/0.8476	29.33/0.8112	28.93/0.8671	34.30/0.9494
	IGNN [64]	49512	—	—	34.72/0.9298	30.66/0.8484	29.31/0.8105	29.03/0.8696	34.39/0.9496
	HAN [41]	64346	6534	1014	34.75/0.9299	30.67/0.8483	29.32/0.8110	29.10/0.8705	34.48/0.9500
	NLSA [40]	44747	4579	840	34.85/0.9306	30.70/0.8485	29.34/0.8117	29.25/0.8726	34.57 0.9508
	SwinIR [28]	11937	1026	1238	34.89/0.9312	30.77/0.8503	29.37/0.8124	29.29/0.8744	34.74/0.9518
	ELAN (ours)	8278	874	530	34.90/0.9313	30.80/0.8504	29.38/0.8124	29.32/0.8745	34.73/0.9517
×4	EDSR [29]	43090	2895	360	32.46/0.8968	28.80/0.7876	27.71/0.7420	26.64/0.8033	31.02/0.9148
	SRFBN [27]	3631	7466	551	32.47/0.8983	28.81/0.7868	27.72/0.7409	26.60/0.8015	31.15/0.9160
	RNAN [61]	9255	480	NaN	32.49/0.8982	28.83/0.7878	27.72/0.7421	26.61/0.8023	31.09/0.9149
	RDN [62]	22271	1310	243	32.47/0.8990	28.81/0.7871	27.72/0.7419	26.61/0.8028	31.00 0.9151
	OISR [15]	44270	2963	—	32.53/0.8992	28.86/0.7878	27.75/0.7428	26.79/0.8068	—
	RCAN [62]	15592	918	223	32.63/0.9002	28.87/0.7889	27.77/0.7436	26.82/0.8087	31.22/0.9173
	SAN [10]	15861	937	NaN	32.64/0.9003	28.92/0.7888	27.78/0.7436	26.79/0.8068	31.18/0.9169
	IGNN [64]	49513	—	—	32.57/0.8998	28.85/0.7891	27.77/0.7434	26.84/0.8090	31.28 0.9182
	HAN [41]	64199	3776	628	32.64/0.9002	28.90/0.7890	27.80/0.7442	26.85/0.8094	31.42/0.9177
	NLSA [40]	44157	2956	502	32.59/0.9000	28.87/0.7891	27.78/0.7444	26.96/0.8109	31.27/0.9184
	SwinIR [28]	11900	584	645	32.72/0.9021	28.94/0.7914	27.83/0.7459	27.07/0.8164	31.67/0.9226
	ELAN (ours)	8312	494	298	32.75/0.9022	28.96/0.7914	27.83/0.7459	27.13/0.8167	31.68/0.9226

drop compared with the SwinIR-light while reducing the latency from 271ms to 247ms. By utilizing our shifted windows mechanism, the performance remain almost unchanged while the inference speed is decreased from 247ms to 177ms.

We then replace the SA calculation with our proposed ASA, the inference latency is greatly reduced from 177ms to 66ms without losing PSNR/SSIM performance. By employing the GMSA which can efficiently model long-range dependency, the PSNR and SSIM indexes get significantly improved on all five datasets. Specifically, the PSNR increases by 0.21dB and 0.19dB on the Urban100 and Manga109 datasets, respectively, while the latency is only slightly increased by 9ms. This indicates the effectiveness of GMSA over the SA in SwinIR with small fixed window size. Finally, by employing the proposed shared
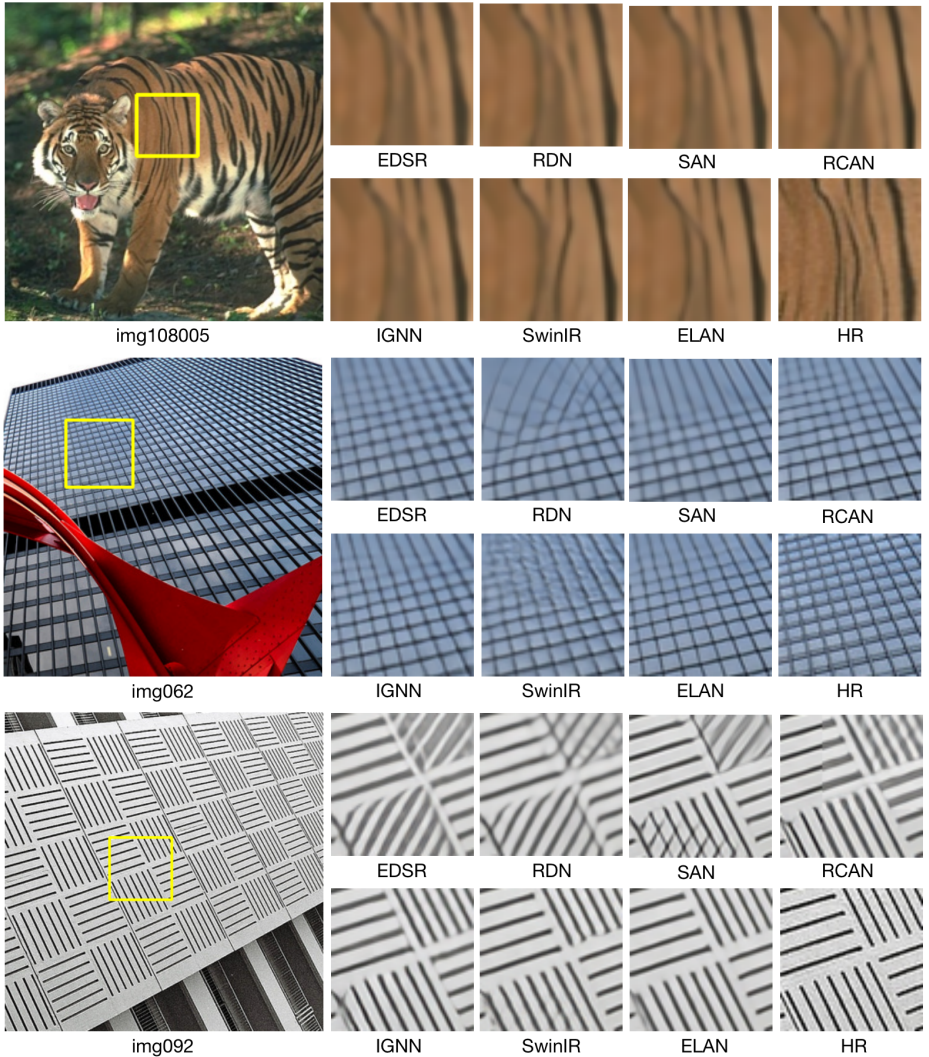
Fig. 5. Qualitative comparison of state-of-the-art classic SR models for ×4 upscaling task. The ELAN can restore more accurate and sharper details than the other models.

attention mechanism, we can further speed up the inference time of ELAN-light with little performance drop. Combining all the improvements, the final version of ELAN-light achieves about ×4.5 acceleration while maintaining comparable performance to SwinIR-light.

Depth of shared attention. We further conduct a detailed ablation study on the depth of shared attention blocks (i.e., n in Figure 2(b)) in sequential layers. ELAN-light is employed for this study and the depth of shared attention blocks varies in $\{0, 1, 3, 5\}$. Note that $n = 0$ means that each ELAB calculates

Fig. 6. Qualitative comparison of state-of-the-art classic SR models for ×4 upscaling task. The ELAN can restore more accurate and sharper details than the other models.

self-attention independently. The results of ELAN-light using different n are reported in Table 4. We also provide one representative CNN-based method EDSR-baseline for intuitive comparison. One can observe that using larger n can effectively reduce the number of network parameters, FLOPs and latency time in the inference stage, at the cost of performance drop. By choosing an appropriate n, our ELAN can achieve a good trade-off between efficiency and performance. It is worth mentioning that even using $n = 5$, the PSNR of ELAN-light on the challenging Urban100 and Manga109 still outperform EDSR-baseline by a large

Table 3. Ablation study on network design for ELAN.

Scale	Model	Different components				#Params (K)	#FLOPs (G)	Latency(ms)	Set5 [3] PSNR/SSIM	Set14 [59] PSNR/SSIM	B100[38] PSNR/SSIM	U100 [17] PSNR/SSIM	Manga109 [39] PSNR/SSIM
		Shifted window	ASA	GMSA	Shared attention								
×4	SwinIR-light [28]					897	49.6	271	32.44/0.8976	28.77/0.7858	27.69/0.7406	26.47/0.7980	30.92/0.9151
	ELAN-light					767	44.6	247	32.38/0.8971	28.68/0.7832	27.62/0.7368	26.40/0.7973	30.78/0.9142
	ELAN-light	✓				765	44.4	177	32.38/0.8971	28.69/0.7833	27.61/0.7367	26.42/0.7973	30.78/0.9141
	ELAN-light	✓	✓			641	43.8	66	32.39/0.8970	28.67/0.7831	27.62/0.7368	26.39/0.7972	30.76/0.9139
	ELAN-light	✓	✓	✓		641	45.5	75	32.47/0.8977	28.79/0.7858	27.71/0.7405	26.60/0.7985	30.95/0.9151
	ELAN-light	✓	✓	✓	✓	601	43.2	62	32.43/0.8975	28.78/0.7858	27.69/0.7406	26.54/0.7982	30.92/0.9150

Table 4. Ablation study on depth selection of shared attention.

Scale	Model	Depth(n)	#Params (K)	#FLOPs (G)	Latency (ms)	Set5 [3] PSNR/SSIM	Set14 [59] PSNR/SSIM	B100[38] PSNR/SSIM	U100 [17] PSNR/SSIM	Manga109 [39] PSNR/SSIM
×4	ELAN-light	0	641	45.5	75	32.47/0.8977	28.79/0.7858	27.71/0.7405	26.60/0.7985	30.95/0.9151
	ELAN-light	1	601	43.2	62	32.43/0.8976	28.78/0.7858	27.69/0.7406	26.54/0.7982	30.92/0.9150
	ELAN-light	3	575	40.4	51	32.35/0.8970	28.71/0.7852	27.65/0.7401	26.40/0.7971	30.74/0.9133
	ELAN-light	5	571	39.3	48	32.31/0.8967	28.66/0.7846	27.62/0.7400	26.35/0.7967	30.63/0.9120
	EDSR-baseline [29]	—	1518	114.0	28	32.09/0.8938	28.58/0.7813	27.57/0.7357	26.04/0.7849	30.35/0.9067

margin (up to 0.31 dB and 0.28 dB, respectively), validating the advantage of modeling long-range attention in our model.

5   Conclusion

In this paper, we proposed an efficient long-range attention network (ELAN) for single image super resolution. The ELAN had a neat topology with sequentially cascaded efficient long-range attention blocks (ELAB). Each ELAB was composed of a local feature extraction module with two sequential shift-conv and a group-wise multi-scale self-attention (GMSA) module to gradually increase the receptive field of self-attention (SA). Benefiting from our accelerated SA calculation and shared attention mechanism, ELAB can effectively capture the local structure and long-range dependency in a very efficient manner. Extensive experiments show that ELAN can obtain highly competitive performance than previous state-of-the-art SR models on both light-weight and performance-oriented settings, while being much more economical than previous transformer-based SR methods. Although our ELAN achieves significant speedup than SwinIR, the calculation of SA is still computation- and memory-intensive compared to those light-weight CNN-based models. In the future, we will further explore more efficient implementations or approximations of SA for more low-level vision tasks.

References

1. Agustsson, E., Timofte, R.: Ntire 2017 challenge on single image super-resolution: Dataset and study. In: Proceedings of the IEEE conference on computer vision and pattern recognition workshops. pp. 126–135 (2017) 3

2. Ahn, N., Kang, B., Sohn, K.A.: Fast, accurate, and lightweight super-resolution with cascading residual network. In: Proceedings of the European Conference on Computer Vision (ECCV). pp. 252–268 (2018) 8, 9

3. Bevilacqua, M., Roumy, A., Guillemot, C., Alberi-Morel, M.L.: Low-complexity single-image super-resolution based on nonnegative neighbor embedding (2012) 8, 13, 16

4. Brown, T., Mann, B., Ryder, N., Subbiah, M., Kaplan, J.D., Dhariwal, P., Neelakantan, A., Shyam, P., Sastry, G., Askell, A., et al.: Language models are few-shot learners. Advances in neural information processing systems 33, 1877–1901 (2020) 2

5. Buades, A., Coll, B., Morel, J.M.: A non-local algorithm for image denoising. In: 2005 IEEE Computer Society Conference on Computer Vision and Pattern Recognition (CVPR'05). vol. 2, pp. 60–65. IEEE (2005) 6

6. Caballero, J., Ledig, C., Aitken, A., Acosta, A., Totz, J., Wang, Z., Shi, W.: Real-time video super-resolution with spatio-temporal networks and motion compensation. In: Proceedings of the IEEE Conference on Computer Vision and Pattern Recognition. pp. 4778–4787 (2017) 1

7. Cao, H., Wang, Y., Chen, J., Jiang, D., Zhang, X., Tian, Q., Wang, M.: Swin-unet: Unet-like pure transformer for medical image segmentation. arXiv preprint arXiv:2105.05537 (2021) 4, 6

8. Carion, N., Massa, F., Synnaeve, G., Usunier, N., Kirillov, A., Zagoruyko, S.: End-to-end object detection with transformers. In: European conference on computer vision. pp. 213–229. Springer (2020) 4

9. Chen, H., Wang, Y., Guo, T., Xu, C., Deng, Y., Liu, Z., Ma, S., Xu, C., Xu, C., Gao, W.: Pre-trained image processing transformer. In: Proceedings of the IEEE/CVF Conference on Computer Vision and Pattern Recognition. pp. 12299–12310 (2021) 4

10. Dai, T., Cai, J., Zhang, Y., Xia, S.T., Zhang, L.: Second-order attention network for single image super-resolution. In: Proceedings of the IEEE/CVF conference on computer vision and pattern recognition. pp. 11065–11074 (2019) 2, 3, 10, 12, 13

11. Dong, C., Loy, C.C., He, K., Tang, X.: Image super-resolution using deep convolutional networks. IEEE transactions on pattern analysis and machine intelligence 38(2), 295–307 (2015) 1, 3, 5

12. Dong, C., Loy, C.C., Tang, X.: Accelerating the super-resolution convolutional neural network. In: European conference on computer vision. pp. 391–407. Springer (2016) 1, 3, 5

13. Dosovitskiy, A., Beyer, L., Kolesnikov, A., Weissenborn, D., Zhai, X., Unterthiner, T., Dehghani, M., Minderer, M., Heigold, G., Gelly, S., et al.: An image is worth 16x16 words: Transformers for image recognition at scale. arXiv preprint arXiv:2010.11929 (2020) 2, 4

14. Fedus, W., Zoph, B., Shazeer, N.: Switch transformers: Scaling to trillion parameter models with simple and efficient sparsity. arXiv preprint arXiv:2101.03961 (2021) 2

15. He, X., Mo, Z., Wang, P., Liu, Y., Yang, M., Cheng, J.: Ode-inspired network design for single image super-resolution. In: Proceedings of the IEEE/CVF Conference on Computer Vision and Pattern Recognition. pp. 1732–1741 (2019) 13

16. Huang, G., Liu, Z., Van Der Maaten, L., Weinberger, K.Q.: Densely connected convolutional networks. In: Proceedings of the IEEE conference on computer vision and pattern recognition. pp. 4700–4708 (2017) 3, 5

17. Huang, J.B., Singh, A., Ahuja, N.: Single image super-resolution from transformed self-exemplars. In: Proceedings of the IEEE conference on computer vision and pattern recognition. pp. 5197–5206 (2015) 8, 13, 16
18. Hui, Z., Gao, X., Yang, Y., Wang, X.: Lightweight image super-resolution with information multi-distillation network. In: Proceedings of the 27th ACM International Conference on Multimedia. pp. 2024–2032 (2019) 8, 9
19. Ioffe, S., Szegedy, C.: Batch normalization: Accelerating deep network training by reducing internal covariate shift. In: International conference on machine learning. pp. 448–456. PMLR (2015) 6
20. Kim, J., Kwon Lee, J., Mu Lee, K.: Accurate image super-resolution using very deep convolutional networks. In: Proceedings of the IEEE conference on computer vision and pattern recognition. pp. 1646–1654 (2016) 3, 5
21. Kingma, D.P., Ba, J.: Adam: A method for stochastic optimization. arXiv preprint arXiv:1412.6980 (2014) 5
22. Lai, W.S., Huang, J.B., Ahuja, N., Yang, M.H.: Deep laplacian pyramid networks for fast and accurate super-resolution. In: Proceedings of the IEEE conference on computer vision and pattern recognition. pp. 624–632 (2017) 5
23. LeCun, Y., Bengio, Y., Hinton, G.: Deep learning. nature **521**(7553), 436–444 (2015) 1
24. Ledig, C., Theis, L., Huszár, F., Caballero, J., Cunningham, A., Acosta, A., Aitken, A., Tejani, A., Totz, J., Wang, Z., et al.: Photo-realistic single image super-resolution using a generative adversarial network. In: Proceedings of the IEEE conference on computer vision and pattern recognition. pp. 4681–4690 (2017) 1
25. Li, W., Zhou, K., Qi, L., Jiang, N., Lu, J., Jia, J.: Lapar: Linearly-assembled pixel-adaptive regression network for single image super-resolution and beyond. Advances in Neural Information Processing Systems **33**, 20343–20355 (2020) 8, 9
26. Li, Y., Zhang, K., Cao, J., Timofte, R., Van Gool, L.: Localvit: Bringing locality to vision transformers. arXiv preprint arXiv:2104.05707 (2021) 2, 4
27. Li, Z., Yang, J., Liu, Z., Yang, X., Jeon, G., Wu, W.: Feedback network for image super-resolution. In: Proceedings of the IEEE/CVF Conference on Computer Vision and Pattern Recognition. pp. 3867–3876 (2019) 10, 12, 13
28. Liang, J., Cao, J., Sun, G., Zhang, K., Van Gool, L., Timofte, R.: Swinir: Image restoration using swin transformer. In: Proceedings of the IEEE/CVF International Conference on Computer Vision. pp. 1833–1844 (2021) 2, 4, 6, 7, 8, 9, 11, 12, 13, 16
29. Lim, B., Son, S., Kim, H., Nah, S., Mu Lee, K.: Enhanced deep residual networks for single image super-resolution. In: Proceedings of the IEEE conference on computer vision and pattern recognition workshops. pp. 136–144 (2017) 1, 3, 5, 8, 10, 12, 13, 16
30. Liu, D., Wen, B., Fan, Y., Loy, C.C., Huang, T.S.: Non-local recurrent network for image restoration. Advances in neural information processing systems **31** (2018) 3, 6
31. Liu, J., Tang, J., Wu, G.: Residual feature distillation network for lightweight image super-resolution. arXiv preprint arXiv:2009.11551 (2020) 10
32. Liu, L., Ouyang, W., Wang, X., Fieguth, P., Chen, J., Liu, X., Pietikäinen, M.: Deep learning for generic object detection: A survey. International journal of computer vision **128**(2), 261–318 (2020) 4
33. Liu, Y., Ott, M., Goyal, N., Du, J., Joshi, M., Chen, D., Levy, O., Lewis, M., Zettlemoyer, L., Stoyanov, V.: Roberta: A robustly optimized bert pretraining approach. arXiv preprint arXiv:1907.11692 (2019) 2

34. Liu, Y., Sun, G., Qiu, Y., Zhang, L., Chhatkuli, A., Van Gool, L.: Transformer in convolutional neural networks. arXiv preprint arXiv:2106.03180 (2021) 2, 4
35. Liu, Z., Lin, Y., Cao, Y., Hu, H., Wei, Y., Zhang, Z., Lin, S., Guo, B.: Swin transformer: Hierarchical vision transformer using shifted windows. In: Proceedings of the IEEE/CVF International Conference on Computer Vision. pp. 10012–10022 (2021) 2, 4, 6
36. Lu, Z., Liu, H., Li, J., Zhang, L.: Efficient transformer for single image super-resolution. arXiv preprint arXiv:2108.11084 (2021) 8, 9
37. Luo, X., Xie, Y., Zhang, Y., Qu, Y., Li, C., Fu, Y.: Latticenet: Towards lightweight image super-resolution with lattice block. In: European Conference on Computer Vision. pp. 272–289. Springer (2020) 8, 9
38. Martin, D., Fowlkes, C., Tal, D., Malik, J.: A database of human segmented natural images and its application to evaluating segmentation algorithms and measuring ecological statistics. In: Proceedings Eighth IEEE International Conference on Computer Vision. ICCV 2001. vol. 2, pp. 416–423. IEEE (2001) 8, 13, 16
39. Matsui, Y., Ito, K., Aramaki, Y., Fujimoto, A., Ogawa, T., Yamasaki, T., Aizawa, K.: Sketch-based manga retrieval using manga109 dataset. Multimedia Tools and Applications **76**(20), 21811–21838 (2017) 8, 13, 16
40. Mei, Y., Fan, Y., Zhou, Y.: Image super-resolution with non-local sparse attention. In: Proceedings of the IEEE/CVF Conference on Computer Vision and Pattern Recognition. pp. 3517–3526 (2021) 2, 3, 11, 13
41. Niu, B., Wen, W., Ren, W., Zhang, X., Yang, L., Wang, S., Zhang, K., Cao, X., Shen, H.: Single image super-resolution via a holistic attention network. In: European conference on computer vision. pp. 191–207. Springer (2020) 2, 3, 11, 13
42. Paszke, A., Gross, S., Massa, F., Lerer, A., Bradbury, J., Chanan, G., Killeen, T., Lin, Z., Gimelshein, N., Antiga, L., et al.: Pytorch: An imperative style, high-performance deep learning library. Advances in neural information processing systems **32**, 8026–8037 (2019) 9
43. Radford, A., Narasimhan, K., Salimans, T., Sutskever, I.: Improving language understanding by generative pre-training (2018) 2
44. Ramachandran, P., Parmar, N., Vaswani, A., Bello, I., Levskaya, A., Shlens, J.: Stand-alone self-attention in vision models. Advances in Neural Information Processing Systems **32** (2019) 2, 4
45. Sajjadi, M.S., Scholkopf, B., Hirsch, M.: Enhancenet: Single image super-resolution through automated texture synthesis. In: Proceedings of the IEEE international conference on computer vision. pp. 4491–4500 (2017) 5
46. Sajjadi, M.S., Vemulapalli, R., Brown, M.: Frame-recurrent video super-resolution. In: Proceedings of the IEEE Conference on Computer Vision and Pattern Recognition. pp. 6626–6634 (2018) 1
47. Shi, W., Caballero, J., Huszár, F., Totz, J., Aitken, A.P., Bishop, R., Rueckert, D., Wang, Z.: Real-time single image and video super-resolution using an efficient sub-pixel convolutional neural network. In: Proceedings of the IEEE conference on computer vision and pattern recognition. pp. 1874–1883 (2016) 1, 5
48. Tai, Y., Yang, J., Liu, X.: Image super-resolution via deep recursive residual network. In: Proceedings of the IEEE conference on computer vision and pattern recognition. pp. 3147–3155 (2017) 5
49. Tai, Y., Yang, J., Liu, X., Xu, C.: Memnet: A persistent memory network for image restoration. In: Proceedings of the IEEE international conference on computer vision. pp. 4539–4547 (2017) 3, 5

50. Tao, X., Gao, H., Liao, R., Wang, J., Jia, J.: Detail-revealing deep video super-resolution. In: Proceedings of the IEEE International Conference on Computer Vision. pp. 4472–4480 (2017) 1

51. Timofte, R., Agustsson, E., Van Gool, L., Yang, M.H., Zhang, L.: Ntire 2017 challenge on single image super-resolution: Methods and results. In: Proceedings of the IEEE conference on computer vision and pattern recognition workshops. pp. 114–125 (2017) 8

52. Touvron, H., Cord, M., Douze, M., Massa, F., Sablayrolles, A., Jégou, H.: Training data-efficient image transformers & distillation through attention. In: International Conference on Machine Learning. pp. 10347–10357. PMLR (2021) 2, 4

53. Wang, X., Chan, K.C., Yu, K., Dong, C., Change Loy, C.: Edvr: Video restoration with enhanced deformable convolutional networks. In: Proceedings of the IEEE/CVF Conference on Computer Vision and Pattern Recognition Workshops. pp. 0–0 (2019) 1

54. Wang, X., Yu, K., Wu, S., Gu, J., Liu, Y., Dong, C., Qiao, Y., Change Loy, C.: Esrgan: Enhanced super-resolution generative adversarial networks. In: Proceedings of the European Conference on Computer Vision (ECCV) Workshops. pp. 0–0 (2018) 1

55. Wang, Z., Cun, X., Bao, J., Liu, J.: Uformer: A general u-shaped transformer for image restoration. arXiv preprint arXiv:2106.03106 (2021) 4, 6

56. Wu, B., Wan, A., Yue, X., Jin, P., Zhao, S., Golmant, N., Gholaminejad, A., Gonzalez, J., Keutzer, K.: Shift: A zero flop, zero parameter alternative to spatial convolutions. In: Proceedings of the IEEE Conference on Computer Vision and Pattern Recognition. pp. 9127–9135 (2018) 6

57. Wu, B., Xu, C., Dai, X., Wan, A., Zhang, P., Yan, Z., Tomizuka, M., Gonzalez, J., Keutzer, K., Vajda, P.: Visual transformers: Token-based image representation and processing for computer vision. arXiv preprint arXiv:2006.03677 (2020) 4

58. Zamir, S.W., Arora, A., Khan, S., Hayat, M., Khan, F.S., Yang, M.H.: Restormer: Efficient transformer for high-resolution image restoration. arXiv preprint arXiv:2111.09881 (2021) 2, 4

59. Zeyde, R., Elad, M., Protter, M.: On single image scale-up using sparse-representations. In: International conference on curves and surfaces. pp. 711–730. Springer (2010) 8, 13, 16

60. Zhang, Y., Li, K., Li, K., Wang, L., Zhong, B., Fu, Y.: Image super-resolution using very deep residual channel attention networks. In: Proceedings of the European conference on computer vision (ECCV). pp. 286–301 (2018) 1, 2

61. Zhang, Y., Li, K., Li, K., Zhong, B., Fu, Y.: Residual non-local attention networks for image restoration. arXiv preprint arXiv:1903.10082 (2019) 10, 13

62. Zhang, Y., Tian, Y., Kong, Y., Zhong, B., Fu, Y.: Residual dense network for image super-resolution. In: Proceedings of the IEEE conference on computer vision and pattern recognition. pp. 2472–2481 (2018) 3, 5, 10, 12, 13

63. Zheng, S., Lu, J., Zhao, H., Zhu, X., Luo, Z., Wang, Y., Fu, Y., Feng, J., Xiang, T., Torr, P.H., et al.: Rethinking semantic segmentation from a sequence-to-sequence perspective with transformers. In: Proceedings of the IEEE/CVF conference on computer vision and pattern recognition. pp. 6881–6890 (2021) 4

64. Zhou, S., Zhang, J., Zuo, W., Loy, C.C.: Cross-scale internal graph neural network for image super-resolution. Advances in neural information processing systems 33, 3499–3509 (2020) 2, 11, 13